




Hydrodynamically enhanced thermal transport due to strong interlayer interactions: A case study of strained bilayer graphene

Fuqing Duan ¹, Chen Shen ², Hongbin Zhang,² and Guangzhao Qin ^{1,*}¹State Key Laboratory of Advanced Design and Manufacturing for Vehicle Body, College of Mechanical and Vehicle Engineering, Hunan University, Changsha 410082, People's Republic of China²Institut für Materialwissenschaft, Technische Universität Darmstadt, Darmstadt 64289, Germany

(Received 7 September 2021; revised 18 February 2022; accepted 22 February 2022; published 9 March 2022)

Manipulating interlayer interactions in two-dimensional (2D) materials is a widely used and effective method for regulating heat transport, which is important for thermal management of electronics. In this paper, we find that thermal transport can be enhanced by strong interlayer interactions. For instance, 2D bilayer materials with interlayer bonding have larger thermal conductivity than their monolayer counterparts. To further verify the conjecture, we take bilayer graphene (BLG) as a study case to gradually strengthen the interlayer interactions in BLG by applying a series of compressive strains along the out-of-plane direction. It is found that the thermal conductivity of BLG first decreases and then anomalously increases when the strain is larger than the threshold of 12%. For the decreasing trend, it is mainly due to the strain-induced reduction of phonon group velocity and lifetime. While at larger strain ($>12\%$), the anomalous increase of thermal conductivity is found to be caused by hydrodynamic phonon transport and weak phonon anharmonicity. Thus, enhanced interlayer interactions can enhance the hydrodynamic phonon transport and thus improve the heat transfer performance. In this paper, we not only report the hydrodynamic enhancement of thermal transport through enhanced interlayer interactions but also provide solid evidence. These findings will deepen the understanding of thermal transport in layered materials and heterostructures, which will benefit the applications in thermal management.

DOI: [10.1103/PhysRevB.105.125406](https://doi.org/10.1103/PhysRevB.105.125406)

I. INTRODUCTION

Two-dimensional (2D) materials, represented by graphene, have been widely studied and applied to the thermal management of electronic devices in recent years. To adapt to the application of thermal management in practical electronic devices, there are lots of methods proposed, such as defect and disorder [1–3], structure regulation [4–7], doping [8], alloying [9], isotope [10], strain engineering [11], and electric field substrate [12]. Recently, Sun *et al.* [13] have demonstrated that the thermal conductivity of bilayer graphene (BLG) and graphite can be greatly regulated by manipulating interlayer interactions. The out-of-plane compressive strains were applied to manipulate interlayer interaction; $>\frac{1}{4}$ decrease of in-plane thermal conductivity can be achieved by only 6% compressing deformation. Moreover, interlayer interactions also widely exist in heterostructures [14], which have attracted a lot of attention due to their fantastic applications. Thus, it is in demand to study the effect of interlayer interactions on thermal transport, which is of great significance to the applications in many fields, such as electronics, thermoelectrics, and catalysis.

To explore the influence of interlayer interaction, the thermal conductivity of a series of 2D materials from monolayer to bilayer is systematically investigated. As collected in Fig. 1, the thermal conductivities of bilayer silicene, bilayer GaN,

and monolayer/BLG are calculated in this paper, and the others are from the literature [15–22], where MoS₂, MoSe₂, and BN are from experimental measurements. It is shown that bilayer materials with interlayer bonds have larger thermal conductivity than their monolayer counterparts. The other six 2D materials show lower thermal conductivity of the bilayer [with interlayer van der Waals (vdW) interaction] than their monolayer counterparts. By summarizing the results, it is speculated whether the stronger the interlayer interactions, the higher the thermal conductivity.

To test our conjecture, it is necessary to reconcile the interlayer interactions and check the effect on thermal transport. Benefiting from its continuous and robust effects, strain engineering has been widely used to regulating electronic [23,24], thermal [25,26], and optic [24] properties. The effective regulation can be understood in terms of the atomic structure at the nanoscale. For instance, the structure of a material can be changed by strain engineering, so that the interaction between atoms will be strengthened or weakened. As a result, the relevant properties can be regulated accordingly. Thus, strain engineering can also be used to regulate the interlayer interactions.

Considering that different materials process different interlayer interactions, we choose the simplest system of BLG to study the effect of interlayer interaction on thermal conductivity. Strain engineering is employed to investigate how the thermal conductivity varies with interlayer interactions. BLG is a layered material with vdW interactions between two graphene sublayers [13]. Thus, it would be practical to

*Corresponding author: gzqin@hnu.edu.cn

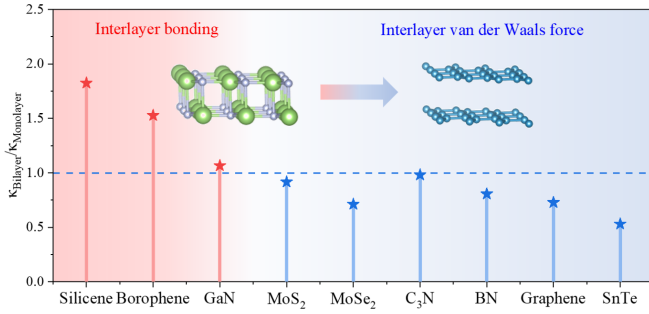


FIG. 1. The normalized thermal conductivity ($\kappa_{\text{Bilayer}}/\kappa_{\text{Monolayer}}$) of silicene, borophene [16], and GaN with interlayer bonding, and MoS₂ [15], MoSe₂ [15], C₃N [17], BN [18], graphene, SnTe [19,20], and SnSe [21,22] with interlayer nonbonding van der Waals interactions. The insert shows sketches of bilayer materials with and without interlayer bonding.

apply a series of out-of-plane compressive strains to BLG to regulate the strength of interlayer interactions. The change in thermal conductivity can then be studied. It is found that the thermal conductivity of BLG first decreases with increasing interlayer interactions and paradoxically increases when the strain is greater than a certain threshold. Commonly, the decrease phenomenon can be understood by analyzing the strain-modulated phonon mode level properties and phonon scattering processes, while the increased thermal conductivity is found to be strongly related to hydrodynamic phonon transport [27].

The hydrodynamic phonon transport process is different from traditional diffusive and ballistic transport under size limit, which has been discovered in bulk materials ~ 50 years ago, but this phenomenon was found to be prominent mainly at ultralarge temperatures [28–30]. Recently, this phenomenon has been computationally observed in 2D materials, such as graphene, boron nitride, fluorographene, and molybdenum disulphide, even at room temperature [31]. In the hydrodynamic region, phonon transport has the same macroscopic drift motion as the mass transport in the fluid. Due to the small proportion of Umklapp scattering processes, phonon transport processes are dominated by Normal scattering processes in the hydrodynamic region. The regulation of hydrodynamic phonon transport has been rarely reported.

In this paper, BLG is used as a study case to modulate the interlayer interactions by applying out-of-plane compressive strain. It is found that the strain-enhanced interlayer interactions can induce phonon hydrodynamic transport and thus increase the thermal conductivity of BLG. The content of the paper is organized as follows. In Sec. II, we describe the methods and calculation parameters of first principles and the Boltzmann transport theory. In Secs. III A and III B, the structure differences between the three materials with and without interlayer bonds are discussed, and the thermal conductivity of BLG under compressive strain is shown. In Secs. III C and III D, the mode level phonon properties and phonon scattering processes are explored to explain the reduction of thermal conductivity. In Sec. III E, the evidence is presented that the hydrodynamic phonon transport is the main reason for the increase in thermal conductivity at large strain ($>12\%$). In

Sec. III F, the phonon anharmonicity and charge density differences are further studied for a deep understanding. Finally, in Sec. IV, a summary and conclusions are provided. In this paper, we deepen the understanding of thermal transport in layered materials and heterostructures, which will benefit the applications of high-performance thermal management.

II. COMPUTATIONAL METHODOLOGY

All first-principles calculations are performed by the Vienna *Ab initio* Simulation Package (VASP) [32] based on density functional theory (DFT). The projector augmented wave method [33,34] is used to describe the electron-ion interaction, and the Perdew-Burke-Ernzerhof (PBE) [35] exchange-correlation functional is employed in this paper for all calculated systems of BLG, silicene, and GaN. In addition, the optB86b [36,37] exchange-correlation function is adopted to consider the interlayer vdW interaction effect in BLG. The cutoff energy is set to 800 eV for BLG at all compressive strains for a good convergence of electronic and ionic during structure optimization. For silicene and GaN, the cutoff energy is set as 800 and 1000 eV, respectively. The Monkhorst-Pack [38] k -mesh of $14 \times 14 \times 1$ is used to sample the irreducible Brillouin zone (BZ) to ensure the accuracy of the calculations. A large vacuum of 20 Å is used to prevent interactions between the other layers due to the periodic mirroring along with out-of-plane directions. The energy convergence accuracy of 10^{-8} eV is employed for geometric optimization with the Hellmann-Feynman force convergence criteria being 10^{-6} eV/Å. The supercell-based method [39–41] is adopted for the calculations of the second and third orders of interatomic force constants (IFCs), and the $5 \times 5 \times 1$ supercell containing 100 atoms is used for all the bilayer systems. Based on the full test of convergence, the cutoff distance is set to 10th nearest neighbors, and $57 \times 57 \times 1$ of Q-grid is used in the calculations of thermal conductivity.

By solving the Boltzmann transport equation (BTE), the lattice thermal conductivity (κ), as well as phonon properties, are calculated as implemented in SHENGBTE [42]. By iteratively solving the linearized BTE [43], the thermal conductivity $\kappa^{\alpha\beta}$ can be expressed as

$$\kappa^{\alpha\beta} = \frac{1}{k_B T^2 \Omega N} \sum_{qv} n_0(n_0 + 1) (\hbar \omega_{qv})^2 v_{qv}^\alpha v_{qv}^\beta \tau_{qv}, \quad (1)$$

where α and β denote the Cartesian components of x , y , or z , k_B is the Boltzmann constant, T and Ω are the absolute temperature and the volume of the unit cell, respectively, N represents the number of discrete q samples in the BZ, qv is a phonon mode of the v branch at the q point, τ_{qv} denotes phonon relaxation time (lifetime), and v_{qv} is the phonon group velocity.

To quantify the specific interlayer interactions, we calculate the interlayer force constants (ILFCs) [44,45] by summing the interatomic force constants of all the atoms from two adjacent layers, which can be expressed as

$$K_{AB} = \sum_{a,b} D_{ab}, \quad (2)$$

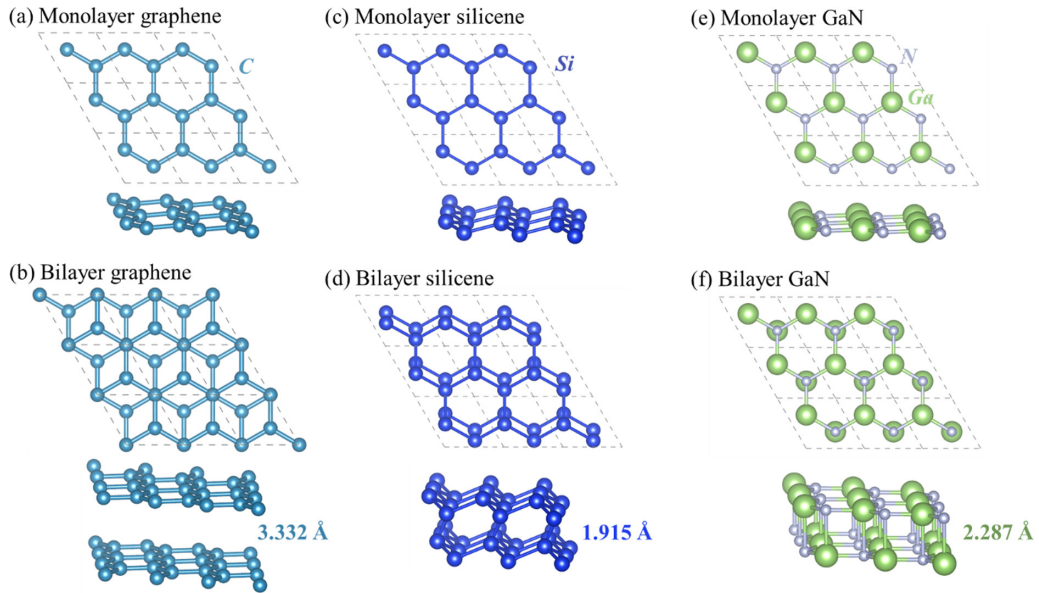


FIG. 2. The top and side views of the geometry structure of (a) and (b) monolayer and bilayer graphene, (c) and (d) silicene, and (e) and (f) GaN. The light blue, navy blue, green, and gray balls represent C, Si, Ga, and N atoms, respectively, which are also marked on site.

where D is the matrix of interatomic force constants, and a and b denote atoms in layers A and B, respectively.

III. RESULTS AND DISCUSSION

A. Effect of strong interlayer interactions

The optimized geometry structures of monolayer and BLG, silicene, and GaN from the top and side views are shown in Fig. 2. For graphene, theoretically, there are two basic types of bilayer structures, namely, AA and AB types. Since the AA structure of BLG is unstable at room temperature, we use the AB type in this paper. It is the interlayer vdW interactions that binds two graphene sheets to form a BLG, as shown in Figs. 2(a) and 2(b). However, for silicene and GaN, there are interlayer bonds connecting and forming the bilayer structures, as shown in Figs. 2(c)–2(f). Note that the structure of bilayer silicene used in this paper is the most stable, which is named slide-2AA according to the work of Fu *et al.* [46]. The lattice constant of graphene is 2.467 Å, which slightly decreases to 2.466 Å when forming BLG. In contrast, the lattice constant of GaN increases slightly from 3.255 Å (monolayer) to 3.328 Å (bilayer). As for silicene, it shows a different behavior that the lattice shape changes when transforming from monolayer ($a = 3.868$ Å) to bilayer ($a = 3.853$ Å and $b = 3.794$ Å). As for the interlayer distance, the vdW distance of BLG (3.332 Å) is larger than that of bilayer silicene (1.915 Å) and GaN (2.287 Å) where bonding is formed. From the monolayer to the bilayer, the lattice thermal conductivity of graphene decreases largely from 3042 to 2215 W/mK. In contrast, the lattice thermal conductivities of silicene and GaN increase from 15.33 and 14.93 W/mK to 27.96 and 18.61 W/mK, respectively. Their common feature is that they all have a honeycomb structure, but strong interlayer bonds are formed in bilayer GaN and silicene when changing from monolayer to bilayer.

To further explore the influence of interlayer interaction, the lattice thermal conductivity of a series of 2D materials from monolayer to bilayer is systematically collected in Fig. 1 from Refs. [15,17–22]. It is shown that the bilayer 2D materials with interlayer vdW interactions show lower thermal conductivity than their monolayer counterparts. By summarizing the results, it can be demonstrated that, with strong interlayer interactions, the thermal conductivity of bilayer materials can be significantly enhanced.

B. Compressive strain-enhanced thermal conductivity

To verify that strong interlayer interactions can enhance thermal conductivity to some extent, it is necessary to tune the interlayer interactions and examine their effects on thermal transport. Taking BLG as an example, we apply a series of compressive strains to BLG along the out-of-plane direction to narrow the interlayer distance. Thus, the interlayer interactions can be modulated, and then we can observe the change in thermal conductivity. When the applied strain increases from 0 to 16%, all phonon dispersions of BLG are free of imaginary frequencies, which indicates the thermodynamic stability of the structure with strain applied. For a clear view, here, we only show the phonon dispersions of BLG in Fig. 3 with a few representative out-of-plane compressive strains applied. It is revealed in the inset of Fig. 3 that the layer-breathing mode (ZO') denotes the opposite vibration phases of C atoms in adjacent layers [47]. The same as previously pointed by Kong *et al.* [48], the phonon dispersion behavior of BLG is very similar to that of monolayer graphene except the ZO' mode. The emerging ZO' in BLG is due to the out-of-phase z -direction vibration of C atoms in adjacent layers, where the close frequency to ZA may result from the weak interlayer interactions. It is also found that all the other phonon branches of BLG are degenerated with small splitting aroused by weak interlayer coupling [49]. With the compressive strain applied, the overall phonon dispersion has little changes except for

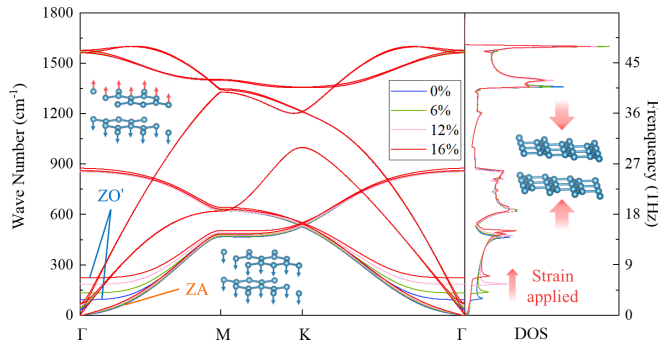


FIG. 3. Phonon dispersion curves and corresponding density of states (DOS) of bilayer graphene under a few representative out-of-plane compressive strains. The displacement patterns of ZA and ZO' are shown in the inset.

ZO' branches. The frequency of out-of-plane ZO' branches increases apparently near the Γ point with the strain increasing, which is due to the strain-enhanced interlayer interactions, leading to the decreasing phonon group velocity. In addition, the density of states (DOS) also shows an increase in ZO' frequency in the phonon dispersion, as shown in Fig. 3. Since it has been reported that the flexural and layer-breathing phonon branches (ZA and ZO') dominate the κ of graphene [50], we focus on the behavior of the two phonon branches. The increasing frequency of ZO' as well as the little changed ZA indicate the decreasing trend of their group velocity with strain applied, which will result in the diminished contribution to the lattice thermal conductivity.

The calculated thermal conductivity of BLG at 300 K as the applied compressive strains increases from 0 to 16% is shown in Fig. 4(a). The results from the iterative method are in good agreement with a previous study [13]. The results from the relaxation time approximation (RTA) method and the results from the iterative method neglecting the effect of Born effective charge and dielectric constants (recorded as “Without Born”) are also plotted for comparison. As clearly shown in Fig. 4(a), there is almost no difference in the black and red curves, and Born effective charge and dielectric constants have little influence on thermal transport even under compressive strain. Surprisingly, the results from the iterative and RTA methods show different behaviors as the strain increases. For the iterative method, the thermal conductivity of BLG decreases monotonously with strain increasing when the strain is $<12\%$. Intuitively, it can be expected that the thermal conductivity of BLG keeps decreasing with larger strain applied. However, the thermal conductivity starts to increase when the strain is $>12\%$. The anomalous increase of thermal conductivity with strain $>12\%$ is highlighted by the red region in Fig. 4(a). However, the results of the RTA method show an almost monotonic increase in thermal conductivity with the increasing compressive strain. The interesting divergence between the results of the iterative and RTA methods is strongly related to hydrodynamic phonon transport, which will be discussed further later.

To observe the change of interlayer interactions with the increasing out-of-plane compressive strain, we calculate the Frobenius norm of the ILFCs of BLG. The normalized ILFCs

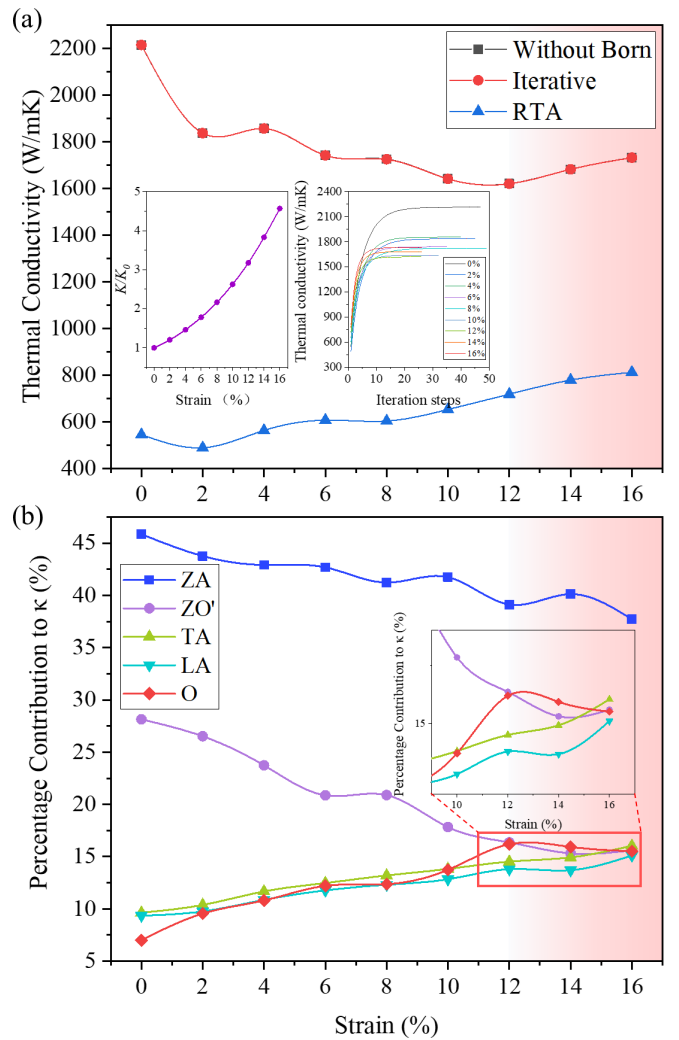


FIG. 4. (a) Thermal conductivity of bilayer graphene as a function of compressive strain along the out-of-plane direction. The results from the iterative method are highlighted in red. The results from the relaxation time approximation method (blue) and the results from the iterative method neglecting the effect of Born effective charges and dielectric constants (without Born; black) are also plotted for comparison. The two insets show the normalized interlayer force constants (ILFCs, K/K_0) as a function of strain and the convergence of thermal conductivity with iteration steps, respectively. (b) Percentage contributions to thermal conductivity (κ) from each phonon branch (ZA, ZO', TA, LA, O) as a function of strain. The inset presents the enlarged partial illustration of the red rectangle.

(K/K_0) are plotted in the left inset of Fig. 4(a), where K_0 means the ILFCs of pristine BLG without strain. As the compressive strain increases, the ILFCs increase monotonously, showing that the compressive strain can indeed modulate the interlayer interactions. The curve shows a quadratic trend with the increasing strain, which indicates that the ILFC is relatively much larger under high compressive strain. Moreover, the right inset of Fig. 4(a) shows the convergence of thermal conductivity of BLG with iteration steps, which confirms the accuracy of the iterative method.

It has been shown that the thermal conductivity of BLG can be enhanced when the interlayer interaction is strong enough,

and the out-of-plane compressive strain $>12\%$. However, two essential questions are still open to be answered. Why does the thermal conductivity of BLG decrease first with increasing compressive strain before increasing paradoxically? What is the fundamental mechanism of the anomalous increase of the thermal conductivity when the strain is $>12\%$?

For the first question, we investigate the percentage contributions to the total thermal conductivity from different phonon branches (ZA, ZO', TA, LA, and O), as shown in Fig. 4(b). The percentage contributions of flexural modes (ZA and ZO') gradually decrease with the increase of strain, especially for ZO' modes. The decreasing contributions to the lattice thermal conductivity from ZA and ZO' are consistent with strain-driven phonon dispersion behavior, as discussed previously referring to Fig. 3. On the contrary, the percentage contributions of the other phonon modes (TA, LA, and O) gradually increase with the increase of strain. Since ZA and ZO' dominate the thermal transport in BLG, the variation of thermal conductivity of BLG keeps pace with ZA and ZO' when strain is $<12\%$. Thus, the decreasing thermal conductivity of BLG with the compressive strain lies in the decreasing contribution of ZA and ZO'.

However, when the strain is $>12\%$, the situation becomes complicated. For a clear view, we enlarge the partial illustration of the mixing region from 12 to 16%, as shown in the inset of Fig. 4(b). The reduction of the percentage contributions of ZA and ZO' branches to the thermal conductivity slows down and even shows some increase. In addition, there is a relatively large surge in the TA and LA branches but a jump in the optical phonon (O) branches. Considering the combined effect of the complex contributions from different phonon branches, the increase of the thermal conductivity with strain $>12\%$ can be understood to a certain extent.

C. Mode level analysis

To further understand the contribution from different phonon branches, the modal phonon group velocity and phonon relaxation time (lifetime) are explored for a detailed analysis. The modal level phonon group velocities of BLG under different compressive strains are shown in Fig. 5(a). As the strain increases, the phonon group velocity decreases monotonously in the low-frequency region, corresponding to the frequency region of ZO', as shown in Fig. 3. Under high compressive strain ($>12\%$), the phonon group velocity starts to increase, which is consistent with the increasing thermal conductivity. Phonon group velocity is calculated based on the slope of the phonon dispersion curve. Thus, the decreasing slope of the ZO' curve corresponds to the decreased phonon group velocity. Considering that the phonon group velocity is proportional to \sqrt{E} [51], where E is Young's modulus, we also check Young's modulus. As shown in the inset of Fig. 5(c), the change of E can verify the overall change of phonon group velocity. Interestingly, the changing curve of E is like the lattice thermal conductivity calculated by the iterative method [Fig. 4(a)]. The decreasing part under 0–12% strain is mainly contributed by ZO', and the increasing part under 12–16% strain corresponds to the overall increasing phonon group velocity. Furthermore, the phonon lifetime of BLG under different compressive strains is plot-

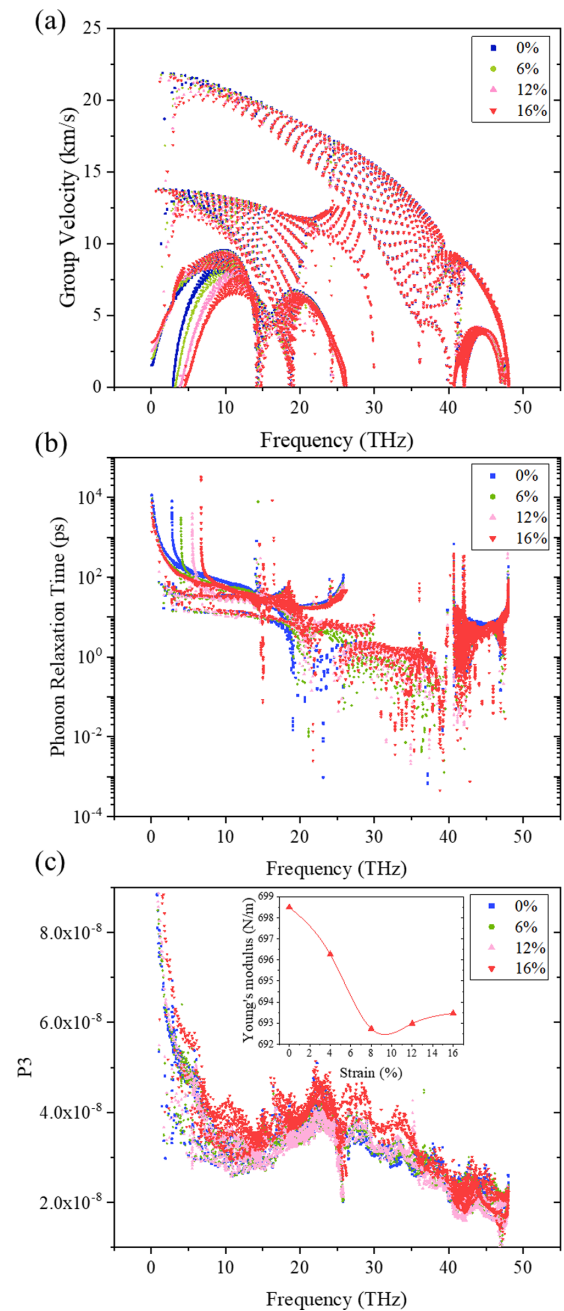


FIG. 5. The modal level (a) phonon group velocity, (b) phonon relaxation time, and (c) phonon scattering phase space (P_3) of bilayer graphene with a few representative compressive strains applied. The inset of (c) presents the strain driven in-plane Young's modulus.

ted in Fig. 5(b). Like the change of phonon group velocity, the phonon lifetime also decreases when the strain is $<12\%$ and then increases when the strain is $>12\%$. Note that the phonon scattering phase space also shares a similar change with phonon lifetime (decreases slightly under 0–12% strain and increases under 12–16% strain), as shown in Fig. 5(c).

D. Decomposed scattering process

To explore the underlying mechanism of the increase of thermal conductivity under large strain, we further apply a

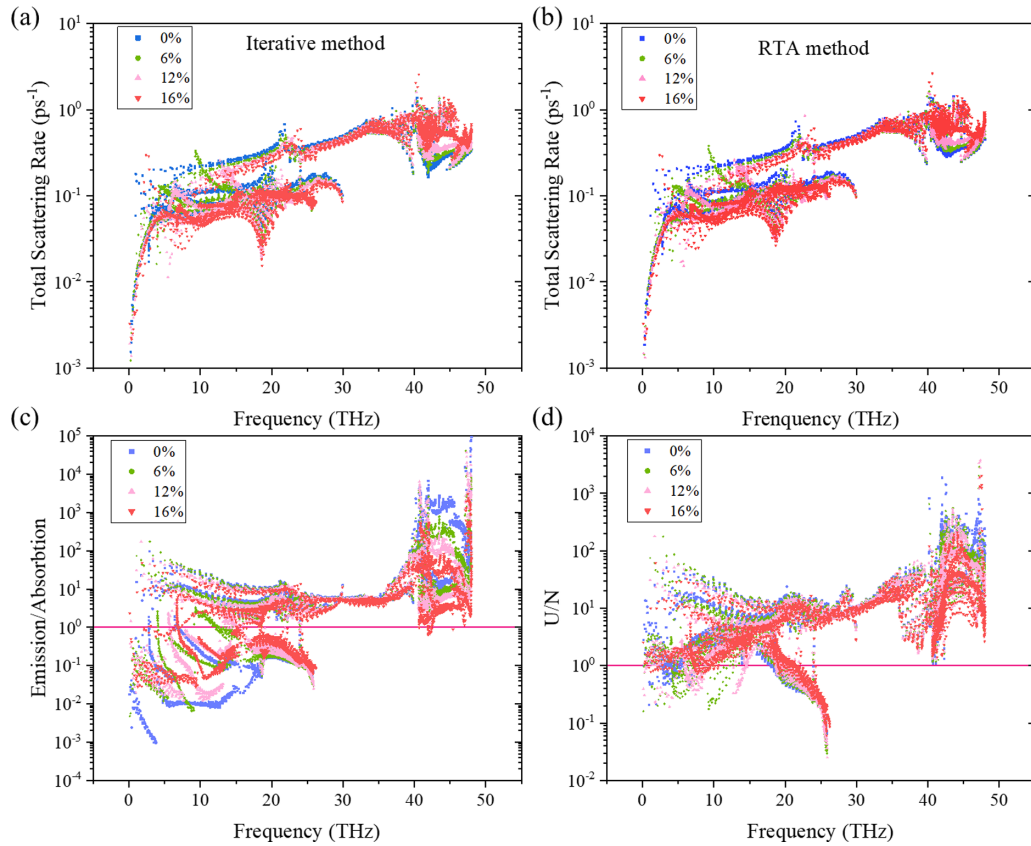


FIG. 6. The modal level scattering rate calculated from (a) the iterative method and (b) the RTA method and the classification of (a) into (c) absorption/emission and (d) Umklapp/Normal (U/N) process of bilayer graphene with a few representative compressive strains applied. The horizon red lines in (c) and (d) mark the equal proportion ratio.

detailed analysis on the phonon-phonon scattering process. The total phonon-phonon scattering rates of BLG under compressive strain calculated by the iterative and relaxation time approximation methods are shown in Figs. 6(a) and 6(b), respectively. The total scattering rate decreases monotonously with the increase of strain, especially at high compressive strains. This reduction in scattering rate means that there are less phonons being scattered as the strain increases, which is beneficial to the thermal transport. Furthermore, we decompose the total phonon scattering rate into emission/absorption and Umklapp/Normal (U/N) processes, the ratios of which are plotted in Figs. 6(c) and 6(d), respectively, for comparison. From Fig. 6(c), the absorption and emission processes are almost equivalent in low-frequency acoustic phonon modes. However, the high-frequency optical phonon modes are mostly scattered during the emission process. As the strain increases, the absorption process gradually increases, although the emission process starts to dominate high-frequency phonon modes.

As for the U/N scattering process, the phonon modes in the overall frequency region are mainly scattered by the U-scattering process, as shown in Fig. 6(d). Note that, for some acoustic phonon modes, the N-scattering process also plays an important role. As the applied strain increases, the whole scattering process gradually drifts to the direction with increasing proportion of the N process, despite that it is still dominated by the U-scattering process. Since the RTA method treats the N-scattering process as resistance (in fact, the N-scattering

process does not provide thermal resistance) and ignores the important role in the hydrodynamic phonon transport [31,52], the thermal conductivity of BLG is largely underestimated by the RTA method, as evidently shown in Fig. 4(a). Thus, the almost opposite trend of thermal conductivity with increasing strain given by the iterative and RTA methods is mainly due to the impact of the N-scattering process, which is strongly relative to the hydrodynamic phonon transport.

E. Hydrodynamic phonon transport

Hydrodynamic phonon transport [27] means a special phonon transport process that differs from traditional diffusive and ballistic transport [53] in extreme cases. During hydrodynamic transport, phonons exhibit macroscopic drift motion like mess transport in fluids. This special transport phenomenon is found mainly at extremely low temperatures and a narrow range of temperatures [28–31]. At low temperatures, the U-scattering process is largely suppressed, and less crystal momentum needs to be destroyed. Correspondingly, the N-scattering process could be stronger than the U-scattering process, which favors the hydrodynamic phonon transport. In the study case of BLG with out-of-plane compressive strain applied because the RTA method does not consider the effect of N-scattering process on the hydrodynamics and even treats it as resistance, the thermal conductivity of BLG increases with the increasing compressive strain. In contrast, when the N-scattering process is fully included in the iterative method,

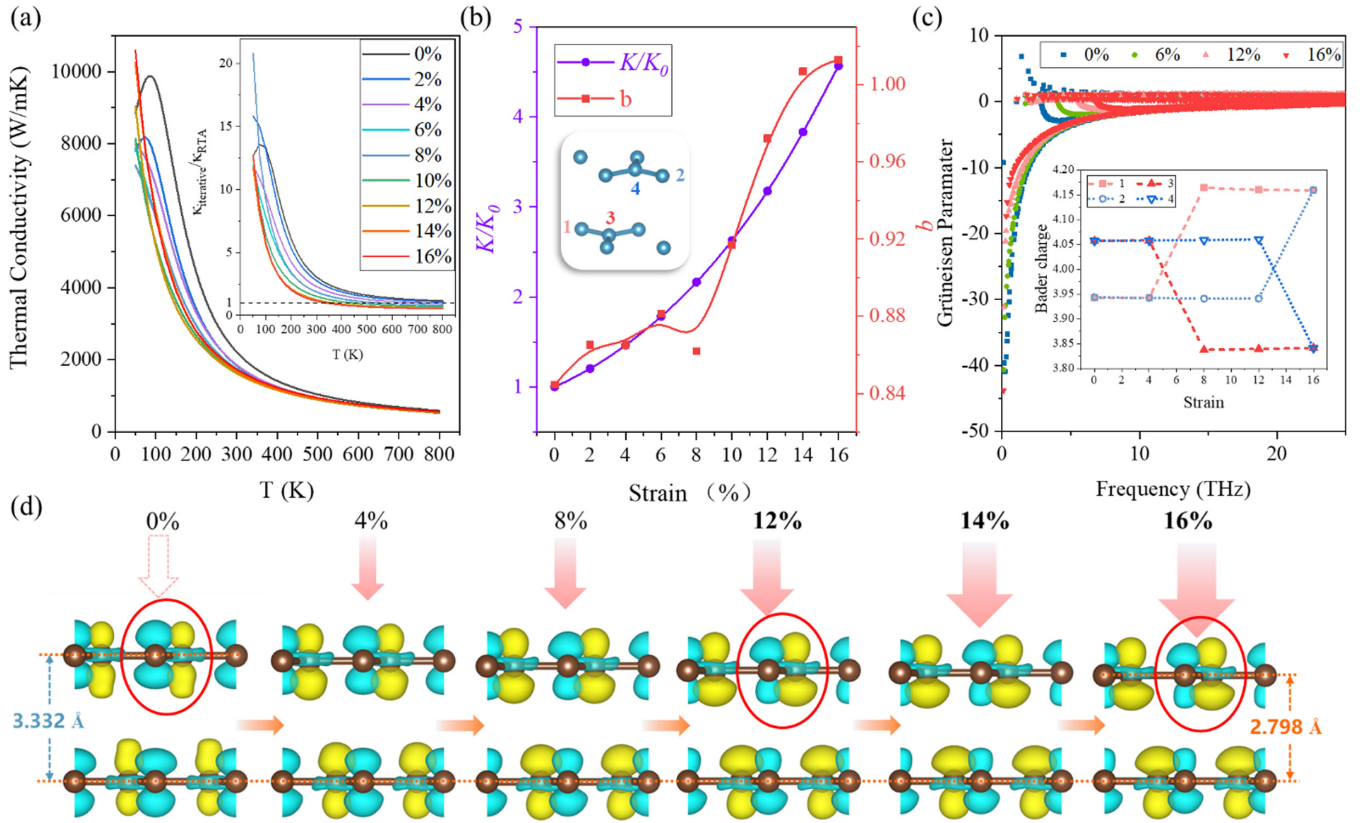


FIG. 7. (a) Thermal conductivity of bilayer graphene (BLG) as a function of temperature under different strains, and the inset shows the change in the ratio of thermal conductivity calculated by the iterative method to that calculated by the RTA method as the temperature increases. (b) The changes of the normalized interlayer force constants (ILFCs, K/K_0) and index b in Eq. (3) with the strain increasing. (c) Comparison of Grüneisen parameter of BLG with a few representative compressive strains applied calculated by the iterative method as implemented in SHENGBTE. (d) The evolution of the charge density difference for BLG with strain increasing calculated by the iterative method as implemented in VASP. The blue and yellow regions represent losing and gaining electrons, respectively. The calculated corresponding Bader charge is shown in the inset of (c), and the structure indicating the atom positions is shown in the inset of (b).

the thermal conductivity firstly decreases and then increases, with a turning point at strain of 12%, as shown in Fig. 4(a). Such a difference between the RTA and iterative methods indicates that the N-scattering process in BLG plays an important role. When the compressive strain is $>12\%$, the scattering process gradually drifts to the N process [Fig. 6(d)], and the N-scattering becomes so significant that the thermal conductivity is further enhanced due to the hydrodynamic phonon transport.

Phonon Poiseuille flow is one of the most important behaviors of hydrodynamic phonon transport because of the phonon macroscopic drift. It has been proved that the increase of the thermal conductivity with the exponent value in temperature larger than that in the ballistic transport case can be a shred of direct evidence for phonon Poiseuille flow [54,55]. As temperature increases, the proportion of the N-scattering process increases, which means phonons will travel a longer distance to the boundary. The long distance of phonon transport indicates the increase of the effective sample size in the calculation formula of thermal conductivity: $\kappa \sim CvL$, where C is the specific heat, v is group velocity, and L is the effective sample size. In addition, L cannot be changed by temperature in the ballistic limit, and the influence of temperature to C and v is the same in both hydrodynamic and ballistic transport.

Thus, the thermal conductivity should increase more rapidly with increasing temperature in the hydrodynamic transport region than the ballistic transport region [52].

To further investigate the hydrodynamic phonon transport, we calculate the temperature-dependent thermal conductivity with different compressive strains applied. As shown in Fig. 7(a), the thermal conductivity of BLG shows obvious enhancement in the low-temperature region, even exceeding that of monolayer graphene at large strain, which indicates strong hydrodynamic phonon transport. However, as the temperature increases, the U-scattering process gradually increases, and more momentum is destroyed. The ratio of thermal conductivity calculated by the iterative method to that calculated by the RTA method gradually decreases to 1 as the temperature increases [inset of Fig. 7(a)], which reveals the decreasing effect of the hydrodynamic phonon transport and the dominance of diffusive transport with strain applied. The thermal conductivity of the BLG under large strain increases only slightly until the temperature reaches 300 K.

The decreasing thermal conductivity with the increasing temperature can be fitted to the formula:

$$\kappa = T^{-b}, \quad (3)$$

where T denotes absolute temperature, and b is the exponent value. The thermal conductivity of BLG decreases exponentially with temperature increasing, in accord with the well-known $\kappa \sim 1/T$ relationship. Figure 7(b) shows the variation of the parameter b with the increasing strain. Meanwhile, the ratio K/K_0 , which denotes the strength of interlayer interactions in BLG, is also plotted for comparison. The parameter b surges at large strains ($>10\%$), which is direct evidence of phonon Poiseuille flow. Thus, the hydrodynamic phonon transport in BLG at high compressive strains is clearly demonstrated. Moreover, it is interesting to note that the two factors K/K_0 and b show almost the same trend with the increasing strain. This phenomenon clearly demonstrates the correlation between the strengthening interlayer interaction and the increase of the parameter b . As a result, the hydrodynamic phonon transport is enhanced with stronger interlayer interactions, which leads to an increased thermal conductivity even at room temperature. The second question posed in Sec. III B has now been completely answered, i.e., the underlying mechanism for the anomalous increase in the thermal conductivity when the strain is $>12\%$ lies in the enhanced hydrodynamics due to the strengthened interlayer interactions.

It is interesting to note that the thermal conductivity increases first and then decreases with the increases of temperature at the low-temperature region, especially when the strain is very small. The reason lies in the competing effect of heat capacity and phonon mean free path (MFP). At low temperatures, there are few phonons excited. The MFP is very large, which is only limited by the crystal size. Thus, the thermal conductivity is governed by the heat capacity, which increases fast following the well-known Debye T^3 law. The T^3 relationship holds in a wide domain up to a significant fraction of the Debye temperature. As temperature goes up beyond the Debye temperature, the heat capacity saturates. Then the thermal conductivity is governed by the phonon MFP, which is limited by the phonon-phonon scattering (mainly through the U process). Based on the phonon gas kinetic theory, the MFP decreases with temperature increasing following the well-known $1/T$ relation. As a result, the phenomenon that the thermal conductivity decreases with increasing temperature in the high-temperature region emerges, and there exists a peak for the thermal conductivity with temperature variation. As the strain increases, the Debye temperature decreases with the decreasing frequency, and the peaks shift to the left, leaving only the peaks at 0 and 2% strain visible, as shown in Fig. 7(a).

F. Phonon anharmonicity and insight from electronic structures

We further calculated the Grüneisen parameter (γ) of BLG at several representative compressive strains, which can be used to quantify the phonon anharmonicity. As shown in Fig. 7(c), the magnitude of γ almost decreases monotonously with increasing strain, especially for low-frequency phonons. As a result, phonon-phonon scattering is weakened due to the weakening phonon anharmonicity, which is consistent with the variation of phonon scattering rate, as shown in Fig. 6(a). When the strain increases beyond 12%, the magnitude of γ drops to a rather low value, which is advantageous to phonon transport. Thus, the extremely weak phonon anharmonicity

is another significant factor contributing to the increase in thermal conductivity of BLG at large compressive strains ($>12\%$).

Insight into phonon anharmonicity and interlayer interactions can be achieved from the analysis of electronic structures. The charge density shows the distribution of electrons in the lattice, while the charge density difference depicts charge transfer (loss or gain electrons) as atoms combine and form a system. Figure 7(d) shows the evolution of charge density difference of BLG with the compressive strain, which is extracted by subtracting two separate graphene sheets from the BLG. It is shown that, when transferring from monolayer to bilayer, the overlapping Carbon atoms (top view) in two layers lose electrons around their upper and lower regions. In contrast, the nonoverlapping Carbon atoms gain electrons in their upper and lower regions but lose electrons in the closely surrounding region. As the strain increases, the distance between two layers become narrower, changing from 3.332 (strain = 0%) to 2.798 Å (strain = 16%). Correspondingly, the region between the layers gaining electrons becomes more and more mellow, expanding in the in-plane direction, while the region between the layers losing electrons shows the opposite change. In addition, it is found that the height difference between the regions of gaining and losing electrons becomes smaller with the applied strain, especially for the interlayer side [Fig. 7(d)]. To show the actual charge transfer, we further calculate the Bader charge. As shown in the inset of Fig. 7(c), one atom gets electrons, and another atom in the same layer loses electrons, which corresponds exactly to the fattening of the yellow ball and the thinning of the blue ball in Fig. 7(d). It is well known that the interactions between atoms are governed by the attraction and repulsion of charges around the atoms. The charge distribution and the charge transfer reflect the overlap of wave function in the lattice, which is directly related to the interlayer interaction and the lattice anharmonicity. Thus, the evolution of charge density difference with the increasing strain reveals the strengthening of interlayer interactions and the weakening of anharmonicity with the increasing compressive strain.

Furthermore, the electronic band structure and the corresponding orbital projected DOS (pDOS) of BLG under different strains are also investigated to understand the behavior of electrons. As shown in Fig. 8, BLG has zero bandgap at the K point and the valence band maximum (VBM) and conduction band minimum lying on the Γ point, which is consistent with previous studies [13,56]. As the strain applied and increased, the bandgap shows no change, and the Dirac cone keeps existing. As seen from the pDOS, all orbitals (s , p_x , p_y , and p_z) contribute to the valence band, with the p_z orbitals forming the Dirac cone and the s , p_x , and p_y forming the covalent bonding between Carbon atoms within one single graphene layer. In contrast, the conduction band is mainly contributed by the p_z orbitals, contributing to the Dirac cone. Such behavior is well consistent with that in graphene.

With the applied out-of-plane compressive strain increasing from 0 to 16%, it is clear from the pDOS that the peak of p_z orbitals moves up and close to the VBM, while the peak of p_x/p_y orbitals shifts down and away from the VBM. Simultaneously, the peak value increases and decreases for the two orbitals of p_z and p_x/p_y , respectively, as marked by the

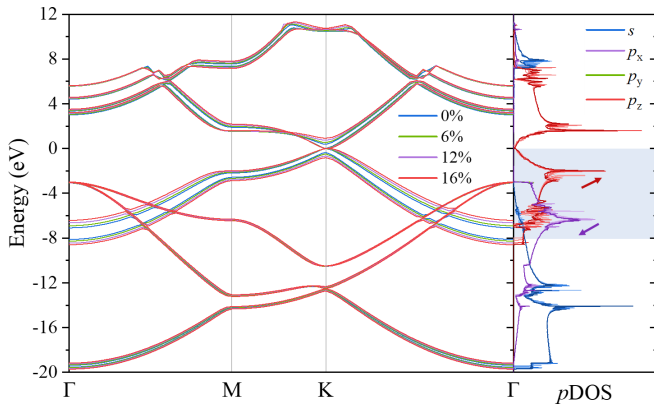


FIG. 8. Electronic band structure and the orbital projected density of states (pDOS) of bilayer graphene with some representative compressive strains applied. For the pDOS, the change in color from light to dark indicates the evolution of pDOS with a gradual increase in strain.

red and violet arrows in Fig. 8. The Dirac cone comes from out-of-plane p_z electrons, and the peaks correspond to the in-plane covalent bond of BLG. When the distance between the two layers decreases with the increasing compressive strain, the out-of-plane charge between layers changes and flattens [Fig. 7(d)], corresponding to the opening of Dirac cone. At the same time, this change affects the in-plane covalent bond, where the bond length becomes longer and the bond strength becomes weaker. The opposite direction of peak shift means that the correlation between the Dirac cone and the covalent bonding becomes weaker with the compressive strain applied. Thus, the correlation between the two single-layer graphene sheets caused by the π bonding in BLG is strengthened, leading to the strengthened interlayer interactions. As a result, the pseudogap (the distance of the two peaks beside the Fermi level) shows a decreasing trend with the strain increasing. In addition, the shift down away from the VBM of the p_x/p_y orbitals, as discussed above, leads to the stronger hybridization with the s orbital. As a result, the covalent bonding in BLG becomes stronger, which is consistent with the shortened bonding length and the corresponding lattice constant. Thus, the anharmonicity in strained BLG is relatively weakened. In short, the evolution of the orbitals is well consistent with the charge distribution and transfer, which explains the strain-strengthened interlayer interactions and weakened anharmonicity.

IV. DISCUSSIONS AND CONCLUSIONS

Based on the above analysis, the underlying mechanisms for the strain-modulated thermal conductivity of BLG can be compiled. The difference in the thermal conductivity calculated from the iterative and RTA methods is termed as $\kappa_{\text{Ite}} - \kappa_{\text{RTA}}$, as shown in Table I. When the strain increases from 0 to 12%, κ_{Ite} decreases, κ_{RTA} increases, and the difference ($\kappa_{\text{Ite}} - \kappa_{\text{RTA}}$) becomes smaller. When the strain continues to increase from 12 to 16%, both κ_{Ite} and κ_{RTA} increase, and the difference remains almost unchanged. To uncover the reason, we first explore phonon group velocity (v_g) and phonon relaxation time (τ). It is found that they both decrease under

TABLE I. Summary table of the approximate changes of various parameters with strain (divided into two parts of 0–12% and 12–16%). Increasing, keeping almost unchanged, and decreasing are denoted by \uparrow , $-$, and \downarrow , respectively.

Relevant parameters	Strain	
	0–12%	12–16%
κ_{Ite}	\downarrow	\uparrow
κ_{RTA}	\uparrow	\uparrow
$\kappa_{\text{Ite}} - \kappa_{\text{RTA}}$	\downarrow	$-$
Group velocity (v_g)	\downarrow	\uparrow
Young's modulus (E)	\downarrow	\uparrow
Phonon relaxation time (τ)	\downarrow	\uparrow
$P3$	$-$	\uparrow
Grüneisen parameter (γ)	\downarrow	\downarrow
N proportion in scattering	$\downarrow \approx \uparrow$	$\downarrow < \uparrow$
Parameter b	$-$	\uparrow

0–12% strain and then increase under 12–16% strain. These changes can explain the change of lattice thermal conductivity of BLG calculated by iterative method well. The change of phonon group velocity can be also revealed by the change of Young's modulus. Considering the group velocity is not directly related to phonon scattering process, we focus on the phonon relaxation time in the following, which is governed by both the phonon phase space and phonon anharmonicity. At the same time, the N proportion also plays a significant role in hydrodynamics. Specifically, the phase space of $P3$ first keeps almost constant and then increases, and the Grüneisen parameter continuously decreases. The variation of these two parameters together determines the variation of relaxation time, which is governed by the Grüneisen parameter. In addition, the difference in the results between the iterative and RTA methods is due to the different treatment of the N process. However, competition exists between the proportion of the N and U processes. The increasing and decreasing of the N proportion are basically equal when the strain is between 0 and 12%, and the increasing N proportion starts to dominate under 12–16% strain [Fig. 6(d)]. The proportion of the N process is closely related to the hydrodynamic phonon transport, which can be revealed by the parameter b . The change of the parameter b (basically constant first and then greatly increased) also confirms the variation of the N process with the strain-modulated interlayer interactions, which explains the anomalously increased thermal conductivity when the strain is $>12\%$.

In summary, we have investigated the thermal conductivity of a series of 2D materials from monolayer to bilayer and find that heat transport can be enhanced by strong interlayer interactions. To test our conjecture, based on first-principles calculations, we apply a series of out-of-plane compressive strains to BLG as a study case to regulate the strength of interlayer interactions. The results show that the thermal conductivity of BLG first decreases and then anomalously increases when the strain is larger than the threshold value of 12%. For the decreasing behavior, the main reasons are the suppression of the phonon group velocity and phonon lifetime caused by the compressive strain. The anomalous

increase in thermal conductivity results from hydrodynamic phonon transport and weak phonon anharmonicity under high strain ($>12\%$). Three phenomena evidently reveal the significant role of hydrodynamic transport: first, the different variation trend of thermal conductivity with strain increasing between the iterative and RTA results; second, the rate of the U/N scattering process gradually drifts to the N-scattering process as the strain increases; and third, the increase in the exponent value of temperature-dependent thermal conductivity, which is a significant indication of phonon Poiseuille flow. The uniformity of the ILFCs, the exponent value b , and the temperature-dependent thermal conductivity intuitively indicate that the strengthened interlayer interaction can indeed enhance the thermal conductivity of BLG. Furthermore, the insight into phonon anharmonicity and interlayer interactions is achieved from the deep analysis of electronic structures. The evolution of the orbitals agrees well with the charge distribution and transfer, which explains the strain-enhancing interlayer interactions and the weakening anharmonicity. When all is said and done, the fact that strong

interlayer interactions can enhance the thermal conductivity of 2D layered materials has been confirmed. We also find the existence of hydrodynamic phonon transport in BLG induced by out-of-plane compressive strains even at room temperature. These findings will deepen the understanding of heat transport in layered materials and heterostructures, which will benefit the applications in thermal management.

ACKNOWLEDGMENTS

This paper is supported by the National Natural Science Foundation of China (Grant No. 52006057), the Fundamental Research Funds for the Central Universities (Grants No. 531119200237 and No. 541109010001), and the State Key Laboratory of Advanced Design and Manufacturing for Vehicle Body at Hunan University (Grant No. 52175011). The numerical calculations have been done on the supercomputing system of the National Supercomputing Center in Changsha.

-
- [1] Y. Gao, Y. Jing, J. Liu, X. Li, and Q. Meng, Tunable thermal transport properties of graphene by single-vacancy point defect, *Appl. Therm. Eng.* **113**, 1419 (2017).
- [2] K. R. Hahn, C. Melis, and L. Colombo, Thermal transport in nanocrystalline graphene investigated by approach-to-equilibrium molecular dynamics simulations, *Carbon* **96**, 429 (2016).
- [3] C. Wang, Y. Liu, L. Li, and H. Tan, Anisotropic thermal conductivity of graphene wrinkles, *Nanoscale* **6**, 5703 (2014).
- [4] M.-H. Bae, Z. Li, Z. Aksamija, P. N. Martin, F. Xiong, Z.-Y. Ong, I. Knezevic, and E. Pop, Ballistic to diffusive crossover of heat flow in graphene ribbons, *Nat. Commun.* **4**, 1734 (2013).
- [5] Z. Ding, In-plane and cross-plane thermal conductivities of molybdenum disulfide, *Nanotechnology* **26**, 065703 (2015).
- [6] F. Liu, R. Zou, N. Hu, H. Ning, C. Yan, Y. Liu, L. Wu, F. Mo, and S. Fu, Enhancement of thermal energy transport across the graphene/h-BN heterostructure interface, *Nanoscale* **11**, 4067 (2019).
- [7] Z. Xiong, X. Wang, K. H. K. Lee, X. Zhan, Y. Chen, and J. Tang, Thermal transport in supported graphene nanomesh, *ACS Appl. Mater. Interfaces* **10**, 9211 (2018).
- [8] Z. Yan, M. Yoon, and S. Kumar, Influence of defects and doping on phonon transport properties of monolayer MoSe₂, *2D Mater.* **5**, 031008 (2018).
- [9] H. Wang, D. Wei, J. Duan, Z. Qin, G. Qin, Y. Yao, and M. Hu, The exceptionally high thermal conductivity after ‘alloying’ two-dimensional gallium nitride (GaN) and aluminum nitride (AlN), *Nanotechnology* **32**, 135401 (2020).
- [10] S. Chen, Q. Wu, C. Mishra, J. Kang, H. Zhang, K. Cho, W. Cai, A. A. Balandin, and R. S. Ruoff, Thermal conductivity of isotopically modified graphene, *Nature Mater.* **11**, 203 (2012).
- [11] H. Xie, T. Ouyang, É. Germaneau, G. Qin, M. Hu, and H. Bao, Large tunability of lattice thermal conductivity of monolayer silicene via mechanical strain, *Phys. Rev. B* **93**, 075404 (2016).
- [12] G. Qin, Z. Qin, S.-Y. Yue, Q.-B. Yan, and M. Hu, External electric field driving the ultra-low thermal conductivity of silicene, *Nanoscale* **9**, 7227 (2017).
- [13] Z. Sun, K. Yuan, Z. Chang, X. Zhang, G. Qin, and D. Tang, Efficient thermal conductivity modulation by manipulating interlayer interactions: a comparative study of bilayer graphene and graphite, *J. Appl. Phys.* **126**, 125104 (2019).
- [14] M.-Y. Li, C.-H. Chen, Y. Shi, and L.-J. Li, Heterostructures based on two-dimensional layered materials and their potential applications, *Mater. Today* **19**, 322 (2016).
- [15] X. Zhang, D. Sun, Y. Li, G.-H. Lee, X. Cui, D. Chenet, Y. You, T. F. Heinz, and J. C. Hone, Measurement of lateral and interfacial thermal conductivity of single- and bilayer MoS₂ and MoSe₂ using refined optothermal Raman technique, *ACS Appl. Mater. Interfaces* **7**, 25923 (2015).
- [16] Y. Yin, Y. Hu, S. Li, G. Ding, S. Wang, D. Li, and G. Zhang, Abnormal thermal conductivity enhancement in covalently bonded bilayer borophene allotrope, *Nano Res.* **11**, 5974 (2021).
- [17] Y. Hong, J. Zhang, and X. C. Zeng, Monolayer and bilayer polyaniline C₃N: two-dimensional semiconductors with high thermal conductivity, *Nanoscale* **10**, 4301 (2018).
- [18] C. Wang, J. Guo, L. Dong, A. Aiyiti, X. Xu, and B. Li, Superior thermal conductivity in suspended bilayer hexagonal boron nitride, *Sci. Rep.* **6**, 25334 (2016).
- [19] D. Zhang, S. Hu, Y. Sun, X. Liu, H. Wang, H. Wang, Y. Chen, and Y. Ni, XTe (X = Ge, Sn, Pb) monolayers: promising thermoelectric materials with ultralow lattice thermal conductivity and high-power factor, *ES Energy Environ.* **10**, 59 (2020).
- [20] A. Pandit, R. Haleoot, and B. Hamad, Thermal conductivity and enhanced thermoelectric performance of SnTe bilayer, *J. Mater. Sci.* **56**, 10424 (2021).
- [21] S. Nag, A. Saini, R. Singh, and R. Kumar, Ultralow lattice thermal conductivity and anisotropic thermoelectric performance of AA stacked SnSe bilayer, *Appl. Surf. Sci.* **512**, 145640 (2020).
- [22] A. Shafique, A. Samad, and Y.-H. Shin, Ultra low lattice thermal conductivity and high carrier mobility of monolayer SnS₂ and SnSe₂: a first principles study, *Phys. Chem. Chem. Phys.* **19**, 20677 (2017).

- [23] V. M. Pereira and A. H. Castro Neto, Strain Engineering of Graphene's Electronic Structure, *Phys. Rev. Lett.* **103**, 046801 (2009).
- [24] R. Roldán, A. Castellanos-Gomez, E. Cappelluti, and F. Guinea, Strain engineering in semiconducting two-dimensional crystals, *J. Phys.: Condens. Matter* **27**, 313201 (2015).
- [25] Y. Zeng, C.-L. Lo, S. Zhang, Z. Chen, and A. Marconnet, Dynamically tunable thermal transport in polycrystalline graphene by strain engineering, *Carbon* **158**, 63 (2020).
- [26] Y. D. Kuang, L. Lindsay, S. Q. Shi, and G. P. Zheng, Tensile strains give rise to strong size effects for thermal conductivities of silicene, germanene and stanene, *Nanoscale* **8**, 3760 (2016).
- [27] J. C. Ward and J. Wilks, III, Second sound and the thermo-mechanical effect at very low temperatures, *Philos. Mag.* **43**, 48 (2009).
- [28] W. Haas and T. Biermasz, The thermal conductivity of KBr, KCl and SiO₂ at low temperatures, *Physica* **4**, 752 (1937).
- [29] B. Bertman and D. J. Sandiford, "Second sound" in solid helium, *Sci. Am.* **222**, 92 (1970).
- [30] L. P. Mezhov-Deglin, Measurement of the thermal conductivity of crystalline He⁴, *Soviet Phys. JETP* **22**, 47 (1966).
- [31] A. Cepellotti, G. Fugallo, L. Paulatto, M. Lazzeri, F. Mauri, and N. Marzari, Phonon hydrodynamics in two-dimensional materials, *Nat. Commun.* **6**, 6400 (2015).
- [32] G. Kresse and J. Furthmüller, Efficient iterative schemes for *ab initio* total-energy calculations using a plane-wave basis set, *Phys. Rev. B* **54**, 11169 (1996).
- [33] G. Kresse and D. Joubert, From ultrasoft pseudopotentials to the projector augmented-wave method, *Phys. Rev. B* **59**, 1758 (1999).
- [34] P. E. Blöchl, Projector augmented-wave method, *Phys. Rev. B* **50**, 17953 (1994).
- [35] J. P. Perdew, K. Burke, and M. Ernzerhof, Generalized Gradient Approximation Made Simple, *Phys. Rev. Lett.* **77**, 3865 (1996).
- [36] J. Klimeš, D. R. Bowler, and A. Michaelides, Chemical accuracy for the van der Waals density functional, *J. Phys.: Condens. Matter* **22**, 022201 (2010).
- [37] J. Klimeš, D. Bowler, and A. Michaelides, Van der Waals density functionals applied to solids, *Phys. Rev. B* **83**, 195131 (2011).
- [38] V. I. Bogdanov, V. A. Popov, V. K. Portnoi, and A. V. Ruban, First-principles investigations of interatomic interactions in Ni₃Al alloyed by interstitial and substitutional impurities, *Phys. Metals Metallogr.* **114**, 191 (2013).
- [39] A. Togo, F. Oba, and I. Tanaka, First-principles calculations of the ferroelastic transition between rutile-type and CaCl₂-type SiO₂ at high pressures, *Phys. Rev. B* **78**, 134106 (2008).
- [40] K. Esfarjani and H. T. Stokes, Method to extract anharmonic force constants from first principles calculations, *Phys. Rev. B* **77**, 144112 (2008).
- [41] X. Tang and J. Dong, Pressure dependence of harmonic and anharmonic lattice dynamics in MgO: a first-principles calculation and implications for lattice thermal conductivity, *Phys. Earth Planet. Inter.* **174**, 33 (2009).
- [42] W. Li, J. Carrete, N. A. Katcho, and N. Mingo, SHENGBTE: a solver of the Boltzmann transport equation for phonons, *Comput. Phys. Commun.* **185**, 1747 (2014).
- [43] G. Qin, Z. Qin, W. Z. Fang, L. C. Zhang, S. Y. Yue, Q. B. Yan, M. Hu, and G. Su, Diverse anisotropy of phonon transport in two-dimensional IV-VI compounds: a first-principles study, *Nanoscale* **8**, 11306 (2016).
- [44] Z.-X. Hu, X. Kong, J. Qiao, B. Normand, and W. Ji, Inter-layer electronic hybridization leads to exceptional thickness-dependent vibrational properties in few-layer black phosphorus, *Nanoscale* **8**, 2740 (2016).
- [45] Y. Zhao, J. Qiao, P. Yu, Z. Hu, Z. Lin, S. P. Lau, Z. Liu, W. Ji, and Y. Chai, Extraordinarily strong interlayer interaction in 2D layered PtS₂, *Adv. Mater.* **28**, 2399 (2016).
- [46] H. Fu, J. Zhang, Z. Ding, H. Li, and S. Meng, Stacking-dependent electronic structure of bilayer silicene, *Appl. Phys. Lett.* **104**, 131904 (2014).
- [47] A. I. Cocemasov, D. L. Nika, and A. A. Balandin, Phonons in twisted bilayer graphene, *Phys. Rev. B* **88**, 035428 (2013).
- [48] B. D. Kong, S. Paul, M. B. Nardelli, and K. W. Kim, First-principles analysis of lattice thermal conductivity in monolayer and bilayer graphene, *Phys. Rev. B* **80**, 033406 (2009).
- [49] K. Sato, J. S. Park, R. Saito, C. Cong, T. Yu, C. H. Lui, T. F. Heinz, G. Dresselhaus, and M. S. Dresselhaus, Raman spectra of out-of-plane phonons in bilayer graphene, *Phys. Rev. B* **84**, 035419 (2011).
- [50] L. Lindsay, D. A. Broido, and N. Mingo, Flexural phonons and thermal transport in graphene, *Phys. Rev. B* **82**, 115427 (2010).
- [51] M. D. Gerboth and D. G. Walker, Effects of acoustic softening on thermal conductivity beyond group velocity, *J. Appl. Phys.* **127**, 204302 (2020).
- [52] S. Lee, D. Broido, K. Esfarjani, and G. Chen, Hydrodynamic phonon transport in suspended graphene, *Nat. Commun.* **6**, 6290 (2015).
- [53] H. Casimir, Note on the conduction of heat in crystals, *Physica* **5**, 495 (1938).
- [54] R. A. Guyer and J. A. Krumhansl, Thermal conductivity, second sound, and phonon hydrodynamic phenomena in nonmetallic crystals, *Phys. Rev.* **148**, 778 (1966).
- [55] R. N. Gurzhi, Thermal conductivity of dielectrics and ferroelectrics at low temperatures, *J. Exptl. Theoret. Phys. (U.S.S.R.)* **46**, 719 (1964) [*Soviet Phys. JETP* **19**, 490 (1964)].
- [56] T. Ohta, A. Bostwick, T. Seyller, K. Horn, and E. Rotenberg, Controlling the electronic structure of bilayer graphene, *Science* **313**, 951 (2006).